A Low-harmonic Control Method of Bi-directional Three-phase Z-source Converters for Vehicle-to-Grid Applications

Wenzheng Xu, Ka Wing Chan, *Member, IEEE*, Siu Wing Or, Siu Lau Ho, Ming Liu

***Abstract*—Three-phase Z-source inverters provide a solution of voltage boosting by a single-stage topology. They are also capable of bi-directional operation as rectifiers, thus have great potential for applications in the field of transportation electrification such as Vehicle-to-Grid (V2G) chargers. In this paper, three new modulation schemes for three-phase Z-source converters are proposed and investigated. The best performed one is further developed to a closed-loop PI control method. While the voltage conversion ratio is flexible, the output voltage Total Harmonics Distortion (THD) is below 3% within the voltage ratio range of 0.5 to 2.5. The effectiveness of the proposed method has been fully validated in MATLAB/Simulink simulations and RT-LAB Hardware-In-Loop (HIL) experiments based on the real-time simulator OPAL-RT OP4510. Compared to existing control methods, the proposed one performs better with reduced harmonics, flexible voltage gain, and simpler control algorithm.**

***Index Terms*—Z-source converter, Bi-directional converter, shoot-through states, voltage harmonics, closed-loop control.**

I. Introduction

THERE is an increasing demand for advanced power converters and their corresponding control algorithms in the field of transportation electrification in general, and railway electrification in specific [1]. Traditional full-bridge three-phase inverter is a fundamental topology for energy transformation between Direct Current (DC) voltage sources such as vehicle batteries and three-phase Alternating Current (AC) power grids, microgrids or loads. However, in the control and operation of traditional full-bridge inverters, dead time between the two switches in the same bridge is required to avoid short-circuit failures [2]. The existence of dead time unavoidably brings AC output waveform distortions. Moreover, when there is a large difference in voltage level between the output AC side and the input DC side, one more DC-DC converter is often added in the inverter to regulate output voltage level. This two-stage system configuration not only decreases the efficiency but also weakens the dynamic response of the system with regard to both disturbances in environmental conditions and grid perturbations [3].

A Z-source inverter [4] and a quasi-Z-source inverter [5] were proposed to overcome the above barriers of traditional two-stage voltage-source inverters. As shown in Fig. 1, an X-shape impedance network composed of two inductors L_{Z1}, L_{Z2} and two capacitors C_{Z1}, C_{Z2} is combined in a traditional three-phase full-bridge inverter [6]. Because of the existence of the X-shape impedance network, it is possible to turn on the two switches in one bridge simultaneously without short-circuited the input voltage source [4]. Moreover, the Z-source inverters take advantage of the shoot-through states ingeniously to achieve voltage boosting without any additional switches or control circuitry [7]. Therefore, the Z-source inverters could achieve voltage buck and boosting by a single-stage topology with high robust. The voltage level of different microgrids could vary considerably, which makes the Z-source converters more advantageous in the process of EV batteries' feeding to the grids. The Z-source inverter could also operate bi-directionally, which is essential in V2G applications. The input diode D_r is connected in parallel with a switch S_1. When switch S_1 is turned on, the Z-source inverter could operate as a conventional three-phase PWM rectifier.

Because of the above-mentioned features, Z-source converters have been widely investigated in areas of not only EV charging [8] [9], but also EV motor drive [10] [11], PV solar energy system [12] [13], wireless energy transfer [14] [15] and integration of microgrid [16] [17]. The increasing voltage gain capability and modulation indexes of both rectifier and inverter stages are advantages of three-phase Z-source converters [18].

Different approaches of applying bi-directional Z-source inverters in V2G applications have been investigated [19] [20]. Paper [21] provided an overall introduction and comparison of space vector modulation schemes for three-phase Z-source inverters. Besides the basic Z-source impedance topology, many modified Z-source topologies have been developed [22]-[24] to reduce switching loss and improve power density. Though these proposed converters based on Z-source topology could generally achieve smaller size and wider voltage conversion ratio, they have issues in complicated structure, instability, voltage stress of switches, power level limitation [24] and output harmonics [7] [25]. Therefore, this paper aims to improve the performance of converter by designing and optimizing the control method of a basic three-phase Z-source converter, rather than adding more devices or complicated circuits.

This work was supported by the Research Grants Council of the HKSAR Government (Grant No. R5020-18) and the Innovation and Technology Commission of the HKSAR Government to the Hong Kong Branch of National Rail Transit Electrification and Automation Engineering Technology Research Center (Grant No. K-BBY1). Corresponding author: Prof. Siu Wing Or (email: eeswor@polyu.edu.hk).

W.Z. Xu, K.W. Chan, S.W. Or, S.L. Ho and M. Liu are with Department of Electrical Engineering, The Hong Kong Polytechnic University, Hung Hom, Kowloon, Hong Kong SAR, China (e-mail: wen-zheng.xu@connect.polyu.hk, eekwchan@polyu.edu.hk, eeswor@polyu.edu.hk, eeslho@polyu.edu.hk, leo.m.liu@connect.polyu.hk). W.Z. Xu, S.W. Or, S.L. Ho, and M. Liu are also with the Hong Kong Branch of National Rail Transit Electrification and Automation Engineering Technology Research Center, Hong Kong SAR, China.

This article has been accepted for publication in a future issue of this journal, but has not been fully edited. Content may change prior to final publication. Citation information: DOI 10.1109/TTE.2020.2984420, IEEE Transactions on Transportation Electrification

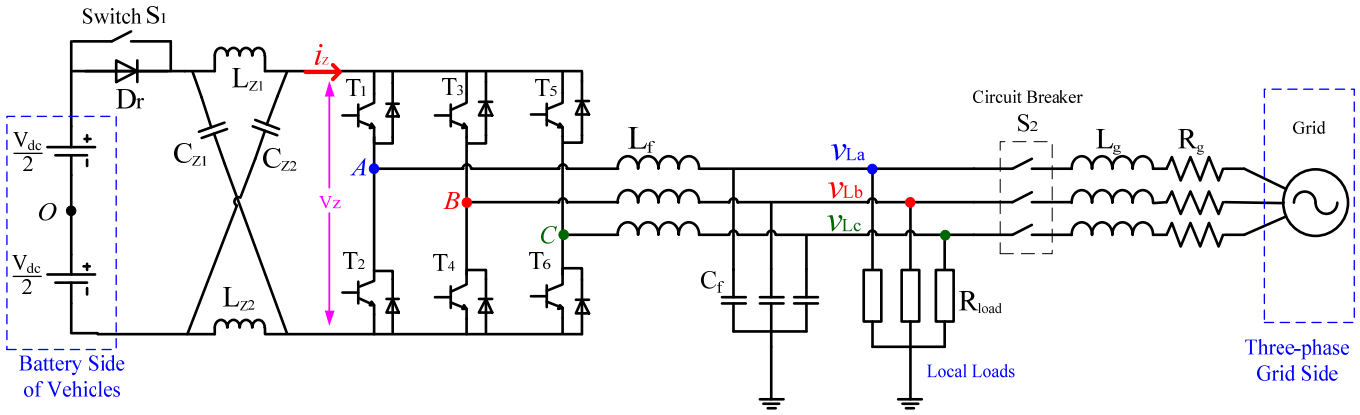

Fig.1 Topology of a bi-directional three-phase Z-source converter

Some advanced control logic for three-phase Z-source converters has been proposed to achieve better dynamic performance [26]-[28], realize ZVS rectifying [29], reduce grid current distortion [30], decouple active and reactive power [3] and increase voltage conversion ratio [31]. However, these control methods require tremendous and complicated calculations to meet the special requirements of designated applications with more passive devices added. Those control schemes are often complicated [32].

In this paper, three new modulation schemes of inserting shoot-through states are proposed. Among them, sine variable modulation shows better performance over harmonic suppression and is therefore further developed into a closed-loop control method. The converter could be connected to the grid or a three-phase load. The switch S_1 and circuit breaker S_2 determine the working mode. To simplify the calculation, the input DC voltage source is divided into two voltage sources, each has the magnitude of $\boldsymbol{V_{dc}}/2$, and the middle point is labelled as $\boldsymbol{O}$. Compared to conventional control schemes, the proposed method in this paper has the following advantages: low harmonics in output voltage and current; support of bi-directional operation; easy to implement without complicated algorithm or computation burden; easy to modify for the control in grid-connected mode.

II. Proposal of Control Methods and Analysis

A. Basic Principle of Three-phase Z-source inverters

Fig. 1 shows the three-phase Z-source inverter which consists of a Z-source topology, a diode D_r and a traditional three-phase full-bridge inverter. The Z-source topology is composed of two inductors L_{Z1}, L_{Z2} and two capacitors C_{Z1}, C_{Z2}. To achieve the symmetrical characteristic, the two inductors usually would have the same inductance, i.e. $L_{Z1}=L_{Z2}=\boldsymbol{L_Z}$, while the two capacitors also would have the same capacitance, i.e. $C_{Z1}=C_{Z2}=\boldsymbol{C_Z}$. Otherwise, an asymmetric topology would lead to unbalanced operation as well as difference in voltage and current stress of devices [33]. The output side of the Z-source topology is connected to a classical three-phase full-bridge inverter with six switches. The diode D_r is placed in series with the DC voltage source to block any reverse current from the Z-source topology in order to achieve voltage boosting [33].

When circuit breaker S_1 is turned on, the converter operates bi-directionally as a rectifier and power transfers from the grid to the DC side of the converter. The Z-source network acts as a special LC filter of the three-phase rectifier. Traditional SPWM control method of three-phase full bridge rectifiers is applicable.

When circuit breaker S_1 is turned off, the converter operates as an inverter and power transfers from the DC side to the three-phase loads or the grid. Circuit breaker S_2 determines whether the converter operates in grid-connected mode or resistive load mode.

The voltage-boosting principle of three-phase Z-source inverters is similar to the one of single-phase ones as described in [33], and therefore the detailed analysis and equivalent circuits in each state are not repeated here. In short, the voltage $\boldsymbol{V_Z}$ is boosted higher than the input voltage $\boldsymbol{V_{dc}}$ because of shoot-through states. In steady state, the operation of Z-source inverter is divided into two periods: shoot-through states and non-shoot-through states [33]. It is assumed that the total time of shoot-through states in one switching cycle is $\boldsymbol{T_s}$, and the period of one cycle is $\boldsymbol{T}$, then the shoot-through duty ratio $\boldsymbol{D}$ of shoot-through states is:

$$D = \frac{T_s}{T} \tag{1}$$

Equation (2) shows the state space equation:

$$\frac{d}{dt}\begin{bmatrix} i_{LZ1}(t) \\ i_{LZ2}(t) \\ v_{CZ1}(t) \\ v_{CZ2}(t) \end{bmatrix} = \begin{bmatrix} 0 & 0 & \frac{2D-1}{L_Z} & 0 \\ 0 & 0 & 0 & \frac{2D-1}{L_Z} \\ \frac{-D}{C_Z} & \frac{1-D}{C_Z} & 0 & 0 \\ \frac{1-D}{C_Z} & \frac{-D}{C_Z} & 0 & 0 \end{bmatrix} \cdot \begin{bmatrix} i_{LZ1}(t) \\ i_{LZ2}(t) \\ v_{CZ1}(t) \\ v_{CZ2}(t) \end{bmatrix} + \begin{bmatrix} \frac{1-D}{L_Z} \\ \frac{1-D}{L_Z} \\ 0 \\ 0 \end{bmatrix} \cdot V_{dc} + \begin{bmatrix} 0 \\ 0 \\ \frac{D-1}{C_Z} \\ \frac{D-1}{C_Z} \end{bmatrix} \cdot i_Z \tag{2}$$

The steady-state parameters could be obtained by setting (2) to zero, as shown in (3):

This article has been accepted for publication in a future issue of this journal, but has not been fully edited. Content may change prior to final publication. Citation information: DOI 10.1109/TTE.2020.2984420, IEEE Transactions on Transportation Electrification

$$\begin{cases} \overline{i_{LZ_1}} = \overline{i_{LZ_2}} = \dfrac{1-D}{1-2D} \cdot \overline{i_Z} \\ \overline{v_{CZ_1}} = \overline{v_{CZ_2}} = \dfrac{1-D}{1-2D} \cdot V_{dc} = \overline{V_Z} \\ v_{Z-peak} = \dfrac{1}{1-2D} \cdot V_{dc} \end{cases} \quad (3)$$

Since ***D*** must be greater than 0 and smaller than 1, the average magnitude of the output voltage across the Z-source topology V_Z is boosted higher than input DC voltage V_{dc} as shown in (3). When more shoot-through states are inserted, the output voltage gain will become higher [34]. The voltage gain of Z-source inverters could be infinite theoretically, whereas the effect of parasitic components and harmonics requirement limit the maximum practical gain.

The core concept of Z-source converter's control is to boost voltage by inserting shoot-through states while reducing output harmonics and power loss [33]. Three shoot-through states inserting methods are proposed below for three-phase Z-source converters.

B. Proposed Modulation Schemes

A study of inverters connected to resistive loads is presented here. Control methods of three-phase Z-source inverters could be classified into two categories: shoot-through of three-phase-leg modulation schemes and shoot-through of single-phase-leg modulation schemes [35]. Each subcategory could be further divided by continuous modulation methods and discontinuous modulation methods. If only one bridge is inserted with shoot-through states, then the high current during shoot-through states would all flow into the two switches of this bridge. Switches of the other two bridges do not share the same current stress, which leads to the asymmetry of the topology and the operation. Therefore, the three-phase-leg modulation scheme is selected for the proposed methods.

In non-shoot-through states, its operation is divided by zero states and non-zero states [35]. Based on this, there are three primary subcategories of inserting shoot-through states: (1) Simple boost control: part of zero states are converted into shoot-through states; (2) Maximum boost control: all zero states areas are converted into shoot-through states; (3) Constant boost control: most of zero states areas are converted into shoot-through states [35] [36]. The proposed methods of inserting shoot-through states are based on conventional SPWM scheme of three-phase full-bridge inverters and belong to constant boost control.

Three sinusoidal modulating signals at the frequency of the desired output but displaced from each other by 2π/3 phase are generated. The triangular carrier wave is compared with the modulation waves to generate six gate signals. The concept is modifying the magnitude of three modulation waves to create overlaps. In Fig. 2(a), the sine modulation waves of generating signals for switch T_1 and T_2 in phase A bridge are presented. The black solid curve represents a standard sine wave whose magnitude ranges from $-M$ to M, where $0 < M < 1$. Two more modulation waveforms are derived by adding a variable ***b(t)*** which varies with time respectively. The red dashed modulation wave is used for generating gate signals for upper switch T_1, which is marked as w_{T1}. The blue dotted modulation wave is used for generating gate signals for lower switch T_2, which is marked as w_{T2}. Fig. 2(b) is a zoomed view of the circled part of Fig. 2(a). It shows the overlap of switching signals G_{T1} and G_{T2} by two different modulation waves. For simplicity, ***b(t)*** is set as a constant in Fig. 2.

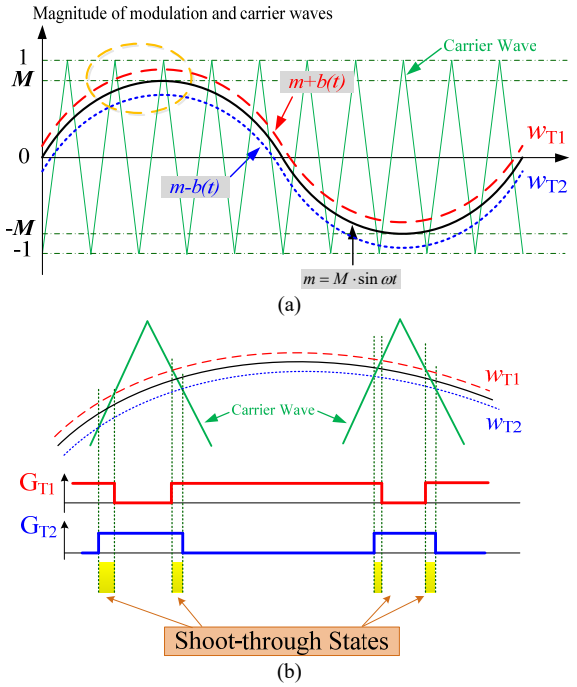

Fig.2 Shoot-through states inserting by overlap: (a) Modulation waves in one cycle; (b) Zoomed view

$$\begin{cases} m_A = M \cdot \sin \omega t \\ m_B = M \cdot \sin(\omega t - \dfrac{2}{3}\pi) \\ m_C = M \cdot \sin(\omega t - \dfrac{4}{3}\pi) \end{cases} \quad (4)$$

The magnitudes of three modulation waves for each bridge are shown in (4), where ***M*** represents the magnitude of sine modulation waves; and m_A, m_B and m_C represent the instantaneous magnitude of modulation waves of phase A, B and C. Both m_A, m_B and m_C range from $-M$ to M. The three modulation waves are compared to the carrier waves in Fig. 2(b), then six pulsed gate signals are generated accordingly as shown in Fig. 3.

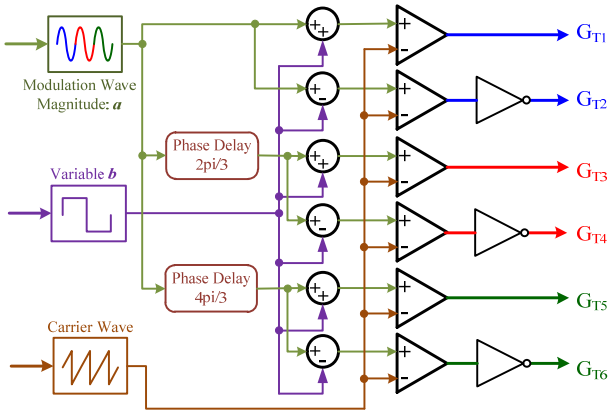

Fig.3 Generation of switching signals to insert shoot-through states

This article has been accepted for publication in a future issue of this journal, but has not been fully edited. Content may change prior to final publication. Citation information: DOI 10.1109/TTE.2020.2984420, IEEE Transactions on Transportation Electrification

The magnitude variation of each modulation wave is marked as a function $b_n(t)$, where n represents the serial number of switches. The modified magnitudes of modulation waves are given in (5), where m_{Au}, m_{Bu} and m_{Cu} represent the instantaneous magnitudes of modulation waves used for generating pulse signals for the upper switches of phase A, B and C, and m_{Al}, m_{Bl} and m_{Cl} represent the instantaneous magnitude of modulation waves used for generating pulse signals for the lower switches of phase A, B and C.

$$\begin{cases} m_{Au} = M \cdot \sin \omega t + b_1(t) \\ m_{Bu} = M \cdot \sin(\omega t - \frac{2}{3}\pi) + b_3(t) \\ m_{Cu} = M \cdot \sin(\omega t - \frac{4}{3}\pi) + b_5(t) \\ m_{Al} = M \cdot \sin \omega t + b_2(t) \\ m_{Bl} = M \cdot \sin(\omega t - \frac{2}{3}\pi) + b_4(t) \\ m_{Cl} = M \cdot \sin(\omega t - \frac{4}{3}\pi) + b_6(t) \end{cases} \quad (5)$$

Fig. 4 shows the modified diagram of space vector modulation. In traditional SVPWM, there are eight vectors and only one switch in a bridge could be turned on. When the state of the upper switch is ON, the state is marked as 1; otherwise, marked as 0. Therefore, there are eight possible combinations of the three bridges' states, i.e. S_0 to S_7. Instead, shoot-through states are feasible for three-phase Z-source inverters. No matter which bridges are inserted with shoot-through states, the voltage V_Z drops to zero, and all the three bridges share the same voltage V_Z. Thus one more vector S_8 is added, which represents the case that shoot-through state is inserted into at least one of the three bridges. The proposed control method belongs to shoot-through of three-phase-leg modulation scheme and continuous modulation method as previously mentioned.

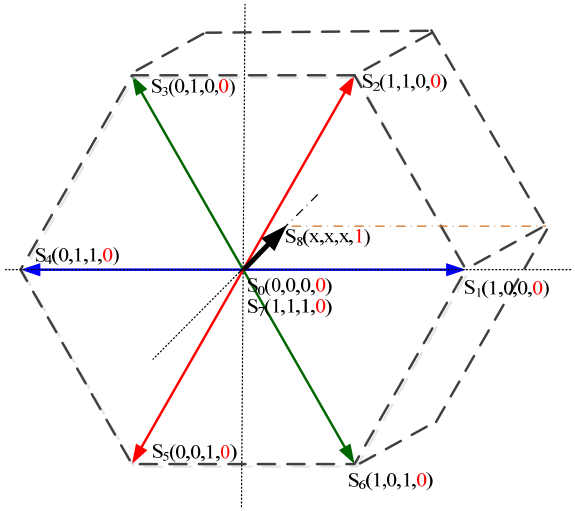

Fig.4 Modified switching vectors

With a variation $b(t)$ of each modulation waves in each bridge, shoot-through states are inserted. Three modulation schemes of defining function $b(t)$ are proposed here: Sine variable modulation, Cosine variable modulation, and Constant variable modulation.

For the sine variable modulation, $b(t)$ is a sine function which has the same phase with the corresponding modulation wave as shown in (6). In this case, the shoot-through states are inserted more in peaks of the modulation wave, and are inserted less in the valleys of the modulation wave. B is a positive constant, and $-B \le b(t) \le B$. The modified modulation waves in one bridge are shown in Fig. 5(a), where the black curve $w_{\sin}$ represents a standard sine waveform, the red curve w_{TU} is modified to generate gate signals for the upper switch, and the blue curve w_{TL} is modified to generate gate signals for the lower switch in the bridge. The green curve shows the magnitude of $b(t)$ over time.

$$\begin{cases} b_1(t) = B \cdot \dfrac{[\sin(\omega t)+1]}{2} & b_2(t) = B \cdot \dfrac{-[\sin(\omega t)+1]}{2} \\ b_3(t) = B \cdot \dfrac{\left[\sin(\omega t - \frac{2}{3}\pi)+1\right]}{2} & b_4(t) = B \cdot \dfrac{-\left[\sin(\omega t - \frac{2}{3}\pi)+1\right]}{2} \\ b_5(t) = B \cdot \dfrac{\left[\sin(\omega t - \frac{4}{3}\pi)+1\right]}{2} & b_6(t) = B \cdot \dfrac{-\left[\sin(\omega t - \frac{4}{3}\pi)+1\right]}{2} \end{cases} \quad (6)$$

For the cosine variable modulation, $b(t)$ is a cosine function which has the same phase with the corresponding modulation waves as presented in equation (7) and Fig. 5(b). In other words, $b(t)$ could be regarded as a sine function which has a $\pi/2$ phase delay with the modulation wave. The shoot-through states are inserted more in valleys of the modulation wave, and are inserted less in the peaks of modulation waves.

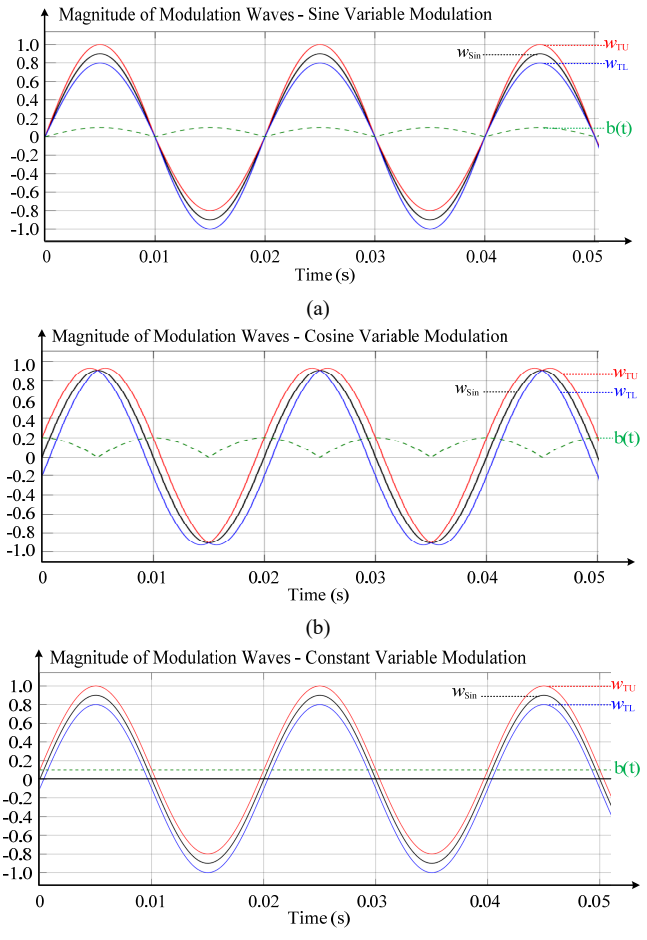

Fig.5 Modulation waves and corresponding magnitudes of $b(t)$: (a) Sine variable modulation; (b) Cosine variable modulation; (c) Constant variable modulation

This article has been accepted for publication in a future issue of this journal, but has not been fully edited. Content may change prior to final publication. Citation information: DOI 10.1109/TTE.2020.2984420, IEEE Transactions on Transportation Electrification

$$\begin{cases} b_1(t)=B\cdot\dfrac{[\cos(\omega t)+1]}{2} & b_2(t)=B\cdot\dfrac{-[\cos(\omega t)+1]}{2} \\ b_3(t)=B\cdot\dfrac{\left[\cos(\omega t-\frac{2}{3}\pi)+1\right]}{2} & b_4(t)=B\cdot\dfrac{-\left[\cos(\omega t-\frac{2}{3}\pi)+1\right]}{2} \\ b_5(t)=B\cdot\dfrac{\left[\cos(\omega t-\frac{4}{3}\pi)+1\right]}{2} & b_6(t)=B\cdot\dfrac{-\left[\cos(\omega t-\frac{4}{3}\pi)+1\right]}{2} \end{cases} \quad (7)$$

For the constant variable modulation, the absolute value of ***b(t)*** is equal to a constant. The constant value is defined as $2\boldsymbol{B}/\pi$ as shown in (8), which is the same with the average magnitude of sine variable modulation as well as cosine variable modulation during one cycle. Thus, it is easy to analyze and compare the three proposed modulation schemes.

$$\begin{cases} b_1(t)=b_3(t)=b_5(t)=\dfrac{2}{\pi}B \\ b_2(t)=b_4(t)=b_6(t)=-\dfrac{2}{\pi}B \end{cases} \quad (8)$$

C. Voltage Gain Analysis

As described before, the input voltage $\boldsymbol{V_{dc}}$ is boosted to $\bar{V}_Z$ by the Z-source topology with the insertion of shoot-through states, then the AC output voltage is higher than the input DC voltage source. The Z-source topology could be regarded as a front-end boost converter for a DC-AC inverter. Bridge voltages $\boldsymbol{V_{AO}}$, $\boldsymbol{V_{BO}}$ and $\boldsymbol{V_{CO}}$ would vary among $+\bar{V}_Z/2$, 0, $-\bar{V}_Z/2$. According to (3), the peak value of phase voltages could be obtained as:

$$\hat{V}_{\mathrm{AO}}=\hat{V}_{\mathrm{BO}}=\hat{V}_{\mathrm{CO}}=\frac{\hat{V}_m}{\hat{V}_{ca}}\cdot\frac{\bar{V}_Z}{2}=M\cdot\frac{\bar{V}_Z}{2}=\frac{M\cdot(1-D)}{1-2D}\cdot\frac{V_{dc}}{2} \quad (9)$$

where $\hat{V}_m$ represents the maximum and peak value of the sine wave. $\hat{V}_{ca}$ represents the peak magnitude of the carrier wave. The modulation ratio is defined as ***M***, which represents $\hat{V}_m/\hat{V}_{ca}$. It is obvious that the shoot-through duty ratio ***D*** in the three proposed modulation schemes is directly determined by ***M*** and ***B***. Because the frequency of the modulation wave is much smaller than that of the carrier wave, the magnitude of modulation wave could be assumed as constant during one switching cycle. Fig. 6 shows the modulation waveforms within a very short time. In Fig. 6, the black line $\boldsymbol{w}_{\mathrm{sin}}$ represents the standard sine waveform, the red line $\boldsymbol{w}_{\mathrm{TU}}$ represents the modified modulation wave to generate gate signals for the upper switch, and the blue curve $\boldsymbol{w}_{\mathrm{TL}}$ represents the modified modulation wave to generate gate signals for the lower switch in the bridge. The green curve $\boldsymbol{w}_{\mathrm{C}}$ represents the carrier wave. During this short period, it is assumed that the magnitudes of each modulation wave are constant. There is another assumption that the switching frequency of carrier wave is high enough to calculate the ideal duty cycle ***D***.

In Fig. 6, the total time length of shoot-through states in one period of the carrier wave is $2\boldsymbol{t}$. The duty ratio of one bridge $\boldsymbol{D}_{\mathrm{B}}$ is equal to $2\boldsymbol{t}/\boldsymbol{T}$. Since there are three bridges in the full-bridge inverter, the total duty ratio ***D*** is equal to $3\boldsymbol{D}_{\mathrm{B}}$. The time slots when shoot-through states are inserted in two or three bridges simultaneously would occur when the instant magnitudes of modulation waves of two bridges are equal or very close to each other. These time slots normally account for very little portion and are thus neglected unless ***B*** is very large. The following equations could be obtained:

$$\frac{r}{t}=\frac{2R}{T} \quad (10)$$

Since $\boldsymbol{R}=2$, $\boldsymbol{r}=4\boldsymbol{B}/\pi$, duty ratio could be obtained as:

$$D=3D_B=3\times\frac{r}{2}=\frac{3}{2}\times\frac{4B}{\pi}=\frac{6B}{\pi} \quad (11)$$

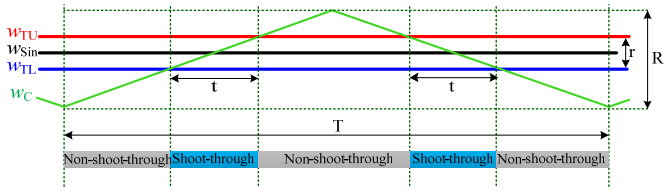

Fig.6 Duty ratio of shoot-through state analysis

By replacing this result in (9), the output phase voltages could be obtained in (12). Table I shows a comparison among the proposed control method and typical control methods [26].

$$\hat{V}_{\mathrm{La}}=\hat{V}_{\mathrm{Lb}}=\hat{V}_{\mathrm{Lc}}=\frac{M\cdot(1-D)}{1-2D}\cdot\frac{V_{dc}}{2}=\frac{M\cdot(\pi-6B)}{\pi-12B}\cdot\frac{V_{dc}}{2} \quad (12)$$

In Fig. 7, the relationship between ideal overall voltage gain ***G*** and parameter ***B*** is presented. The overall voltage gain increases with the increase of modulation index ***M*** and parameter ***B***.

III. Comparison and Closed-loop Control

A. Simulation Results and Comparison

Open-loop simulations have been conducted in Matlab Simulink. The DC side voltage $\boldsymbol{V_{dc}}$ is set as 500V to represent a typical EV battery voltage. The balanced three-phase loads are composed of three resistors whose resistance R_{load} is 112.5Ω in star connection, L_{Z1}=L_{Z2}=280μH, C_{Z1}=C_{Z2}=141μF, L_f=8.95mH, C_f=7μF, AC output frequency f=50Hz. The calculation of these parameters is presented in the Appendix.

TABLE I. Comparison with Conventional Control Methods

	Shoot-through Duty Ratio ***D***	Boosting Factor	Overall Gain ***G***	Capacitor Voltage $\boldsymbol{V_C}$
Simple Boost Control	$1-M$	$\dfrac{1}{2M-1}$	$\dfrac{M}{2M-1}$	$V_{dc}\cdot\dfrac{M}{2M-1}$
Maximum Boost Control	$1-\dfrac{3\sqrt{3}M}{2\pi}$	$\dfrac{\pi}{3\sqrt{3}M-\pi}$	$\dfrac{\pi M}{3\sqrt{3}M-\pi}$	$\dfrac{V_{dc}}{2}\cdot\dfrac{3\sqrt{3}M}{3\sqrt{3}M-\pi}$
Constant Boost Control	$1-\dfrac{\sqrt{3}M}{2}$	$\dfrac{1}{\sqrt{3}M-1}$	$\dfrac{M}{\sqrt{3}M-1}$	$\dfrac{V_{dc}}{2}\cdot\dfrac{\sqrt{3}M}{\sqrt{3}M-1}$
Proposed Variable Control	$\dfrac{6B}{\pi}$	$\dfrac{M\pi}{\pi-12B}$	$\dfrac{\pi-6B}{\pi-12B}\cdot M$	$V_{dc}\cdot\dfrac{(\pi-6B)\cdot M}{\pi-12B}$

This article has been accepted for publication in a future issue of this journal, but has not been fully edited. Content may change prior to final publication. Citation information: DOI 10.1109/TTE.2020.2984420, IEEE Transactions on Transportation Electrification

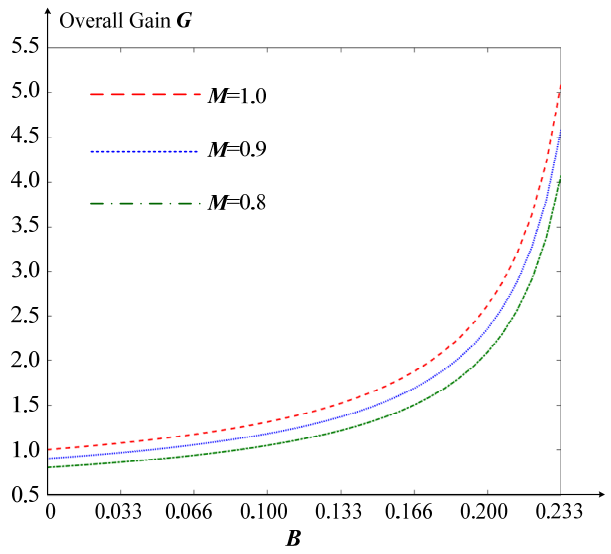

Fig.7 Relationship between the overall gain G and parameter B

First, the simulation at rated output voltage of sine variable method is conducted. The peak magnitude of rated output phase voltage is set as 1060V, whose r.m.s. value is 750V at the medium voltage level. Fig. 8 shows the waveforms of three output phase voltages v_{La}, v_{Lb} and v_{Lc} respectively. The THD of each phase voltage is only 2.66%.

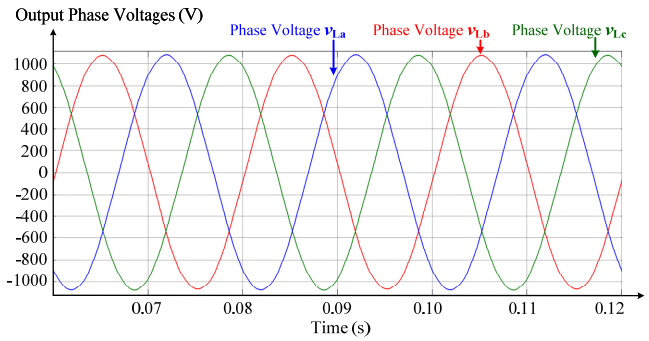

Fig. 8 Output phase voltages of sine variable method at rated output voltage

To further investigate the difference among the three methods on output voltage harmonics, open-loop simulations have been conducted with M=0.9 and B=0.25 such that the magnitude of modified modulation waves would go beyond the magnitude of the carrier wave and the output harmonics would increase undoubtedly. In this way, the effect of the three control methods on output harmonics could be clearly illustrated.

Waveforms of output phase voltages are presented in Fig. 9. It is clear that with such a large value of B, the output harmonic of sine variable method still maintains within a low level. In contrast, the harmonics of cosine variable method is much greater. The harmonics level of constant variable method is slightly lower than one of cosine variable method, but the voltage magnitude is lower than expected. This is because the total duration of the shoot-through states in a three-phase topology has become too long, and the average magnitude of both the capacitor voltage V_{CZ1}, V_{CZ2} and voltage V_Z could not reach the ideal values in (3).

The harmonic analysis plots of three methods are shown in Fig. 10. The cosine variable method produces the highest 5th order harmonics. The 5th, 7th and 11th order harmonics account for most of the total harmonics in the three methods, while there is little even order harmonics because of the symmetricity of the control logic.

Fig. 11(a) represents the relationship between the THD of output phase voltage V_{La} and parameter B when M=0.9. As the magnitude and frequency of output phase voltage V_{La} are the same as V_{Lb} and V_{Lc}, only V_{La} is presented as a representative. The THD increases as B increases because of the shoot-through states insertion. Cosine variable method has the greatest output harmonics, while sine variable method leads to lowest output harmonics.

For sine variable method, the total THD of output phase voltage V_{La} is only 2.83% when B=0.2, which means the magnitude of the modified modulation wave already exceeds the magnitude of the carrier wave. Since the output load is resistive, the voltage distortion and current distortion are the same. For reference, the harmonics of 2nd – 19th orders are compared with the limits in the IEEE 1547 standard [37] as shown in red in Fig. 10(d). It is clear that the output harmonics are well below harmonic limits of the IEEE 1547 standard.

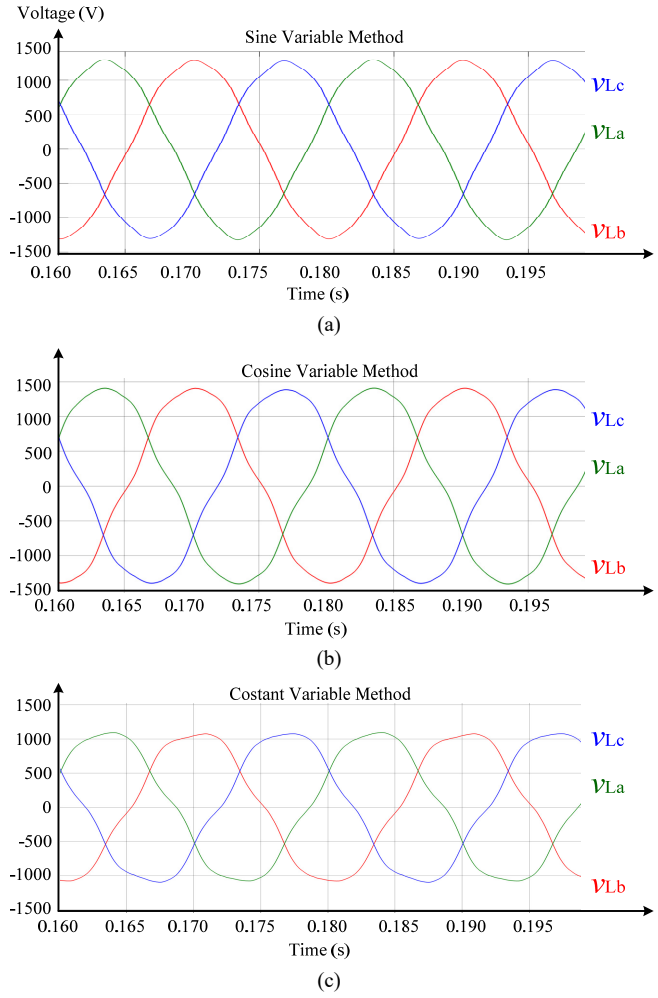

Fig. 9 Waveforms of output phase voltages with high shoot-through duty ratio D: (a) Sine variable method; (b) Cosine variable method; (c) Constant variable method

This article has been accepted for publication in a future issue of this journal, but has not been fully edited. Content may change prior to final publication. Citation information: DOI 10.1109/TTE.2020.2984420, IEEE Transactions on Transportation Electrification

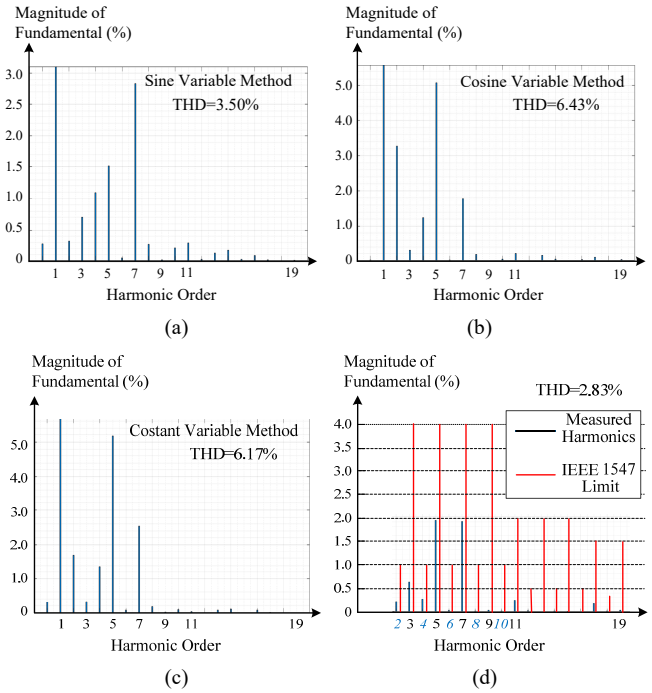

Fig. 10 Harmonics analysis of three proposed control methods when M=0.9 and B=0.25: (a) Sine variable method; (b) Cosine variable method; (c) Constant variable method; (d) Comparison with IEEE 1547 standard harmonics limits

Fig. 11(b) shows the relationship between the output phase voltage magnitude V_{La} and parameter B when M=0.9. Similarly, the output voltage increases as B increases because of the shoot-through states insertion. However, there is no significant difference in the voltage magnitude between three methods because the duty ratio D is the same. The difference between the three modulation schemes is the distribution of shoot-through states insertion, rather than the duty ratio which directly determines the output voltage magnitude. The slight difference of voltage magnitude comes from the fact that when the time of one shoot-through state is too short, the circuit is not able to react and complete the capacitor discharging cycle.

Fig. 11(c) shows the relationship between the THD and the peak magnitude of output phase voltage V_{La}. No matter which control method is selected, the harmonic increases with the voltage magnitude, i.e. the boost ratio, because of more shoot-through states are inserted.

The main difference among the three proposed modulation techniques is the output voltage harmonic, because shoot-through states are inserted in different distribution patterns. In contrast, there is little difference in the output voltage magnitudes of three modulation techniques. The capacitance C_Z and inductance L_Z is determined by defining the voltage ripple ratio and input current limitation as outlined in the Appendix. Since the difference of output voltage magnitudes is little, it is not required to design a different capacitance and inductance for each modulation technique in practical. Meanwhile, only one modulation technique with rated M and B, which suits the working condition the best, would be applied in practical applications.

Regarding to the impact on power loss and efficiency, switching loss would account for most of the total power losses in the three-phase Z-source inverter, as soft switching cannot be easily applied due to its unique feature of inserting shoot-

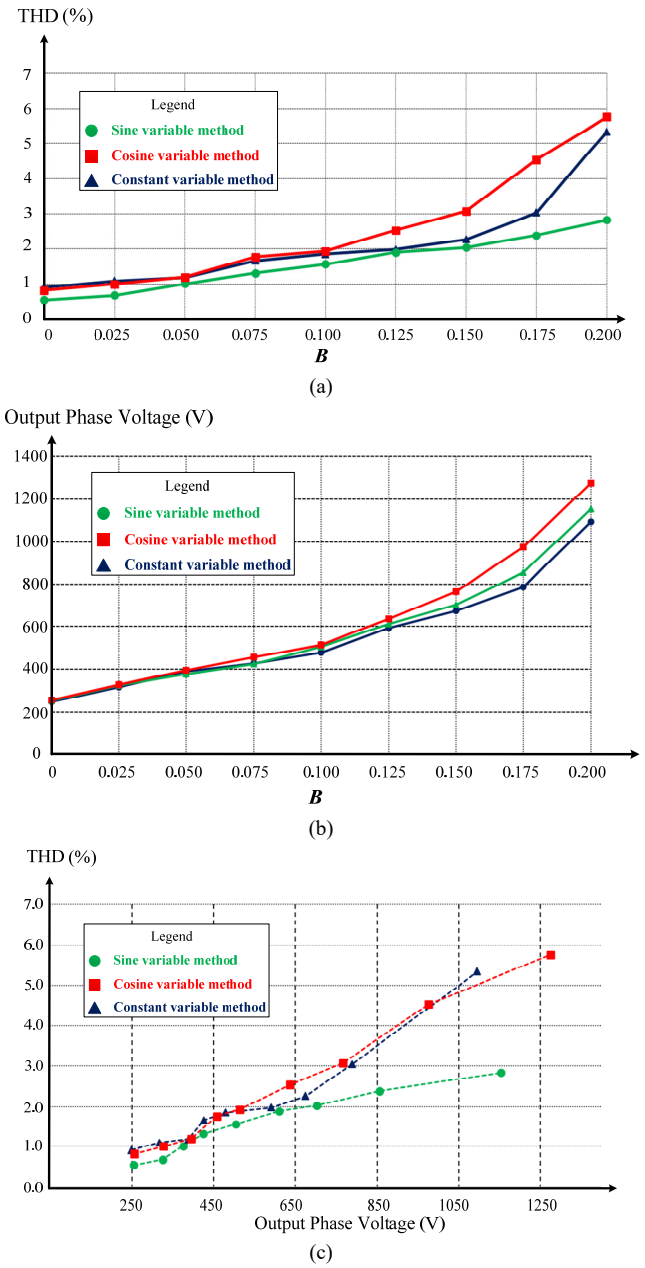

Fig. 11 Comparison of the three proposed control methods: (a) THD of output phase voltages versus B when M=0.9; (b) The magnitude of output phase voltages versus B when M=0.9; (c) THD versus the magnitude of output phase voltages

through states. As mentioned, the main difference among the three modulation schemes is the distribution of the inserted shoot-through states while their switching frequency are the same. Therefore, there is little difference in conversion efficiency among the three modulation schemes.

In summary, sine variable method shows better performance than the other two over harmonics. To further investigate the performance of sine variable method, a series of open-loop simulations are conducted when both M and B vary within the typical operation region. M ranges from 0.6 to 0.95, and B ranges from 0 to 0.2. According to the simulation results, the THD of output voltage always increases with the value of B despite the value of M. However, there is no apparent relationship between THD and the value of M when B is constant.

This article has been accepted for publication in a future issue of this journal, but has not been fully edited. Content may change prior to final publication. Citation information: DOI 10.1109/TTE.2020.2984420, IEEE Transactions on Transportation Electrification

B. *Closed-loop Control Method*

Open-loop simulations are presented above where ***M*** and ***B*** are constant. To achieve closed-loop control, ***M*** and ***B*** shall be calculated according to the measured output voltage via PI control in real-time to ensure that the output voltage magnitude would follow the reference. The dynamic response design process is the same as the one of conventional PI control. The closed-loop control diagram of switching signals generation is presented as shown in Fig. 12.

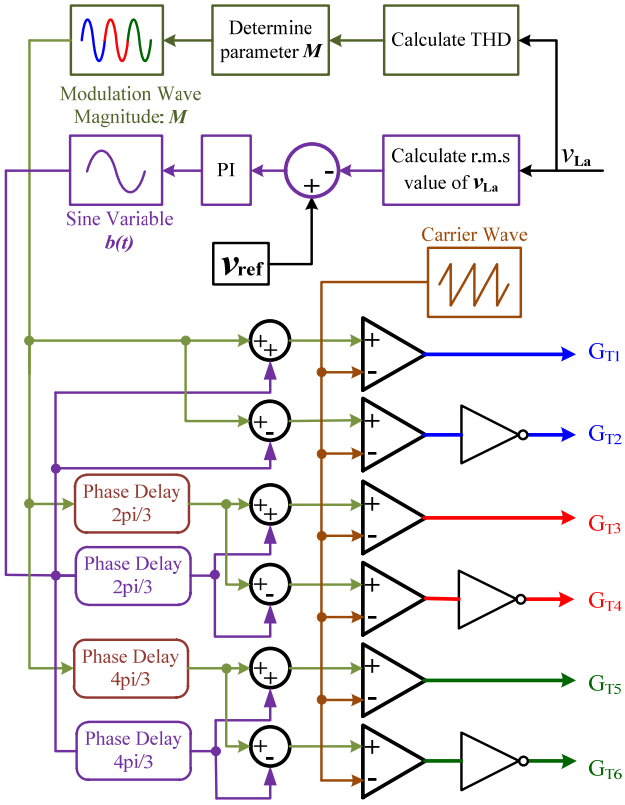

Fig. 12 Generation of switching signals in closed-loop control at balanced load case

Two closed-loop simulations are conducted. First, the reference voltage has a step change from 750V to 900V (r.m.s.), i.e. the peak voltage changes from 1060V to 1273V. Fig. 13 shows that the balanced three phase voltages increased to the new reference smoothly within eight cycles, which takes 0.16s.

Secondly, the resistance R_{load} of each resistive load in star-connection switches from 112.5Ω to 200Ω. As shown in Fig. 14, at the moment of load change when t=0.5s, the output voltage increases for a short time because of the disturbance in load resistance. Then the output voltage is soon regulated and reduced to the rated value 1060V. The output voltage and current become stable within two cycles.

The design of this closed-loop control is based on applying the new sine variable modulation scheme to the traditional closed-loop SPWM PI control methods. There is no modification in the topology of the three-phase Z-source inverter. The common control variable of Z-source inverters is the shoot-through duty ratio ***D***, which is equal to $6B/\pi$ in the proposed modulation schemes. The common output variable of the closed-loop control design is the capacitor voltage V_{CZ1}

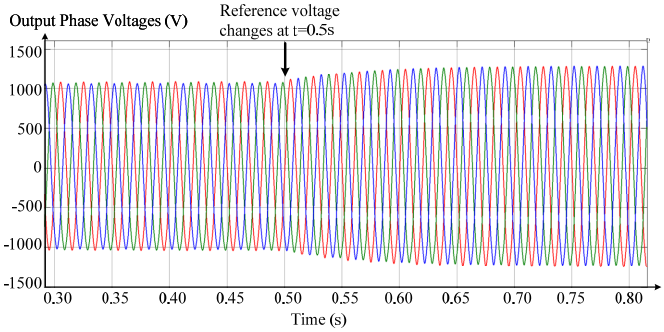

Fig.13 Simulation waveforms when reference voltage changes

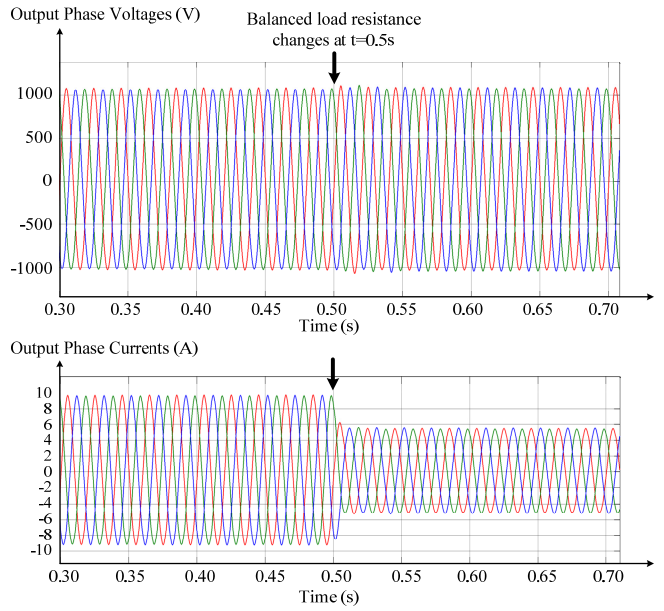

Fig.14 Simulation waveforms of output phase voltages and currents when R_{load} changes

(equal to V_{CZ2}), which directly determines V_Z and output voltage magnitude. Therefore, the methodology of small signal analysis, transfer function and dynamic response design by bode plot of typical three-phase Z-source inverters could be directly adopted in the proposed modulation scheme.

The proposed control could also be easily modified for the operation in grid-connected mode. In conventional SPWM control methods of grid-connected three-phase full-bridge inverters, the magnitude of modulation waves is derived for generating switching signals [38]. The values of parameter ***M*** and ***B*** could be obtained based on the value of S_{abc}. Parameters m_{Au}, m_{Al}, m_{Bu}, m_{Bl}, m_{Cu}, m_{Cl} are thus obtained which represent the magnitudes of modified corresponding modulation waves to insert shoot-through states. The main characteristics of conventional control methods are maintained. It is assumed that the three output phase voltages or three-phase loads are balanced in this paper, thus only phase voltage v_{La} is being measured and calculated for the closed-loop control as shown in Fig. 12. If there is a voltage or load unbalance, only phase voltage v_{La} could catch the reference while the other two phase voltages would vary. Therefore, the proposed closed-loop control method works the best when there is no voltage unbalance present in the connection point to the grid.

This article has been accepted for publication in a future issue of this journal, but has not been fully edited. Content may change prior to final publication. Citation information: DOI 10.1109/TTE.2020.2984420, IEEE Transactions on Transportation Electrification

IV. RT-LAB EXPERIMENT

A. Experimental Setup

The proposed control for three-phase Z-source converter is further verified by Hardware-In-the-Loop (HIL) tests as shown in Fig. 15. The experimental setup is composed of the following: (1) RT-Lab running on OPAL-RT OP4510 simulator; (2) a DSP F28335 control board; (3) a host computer; (4) an oscilloscope. The three-phase Z-source inverter, DC voltage source and resistive load in star connection are simulated in real-time in the RT-Lab. An I/O interface is provided by the RT-Lab for the mutual communication with the DSP control board.

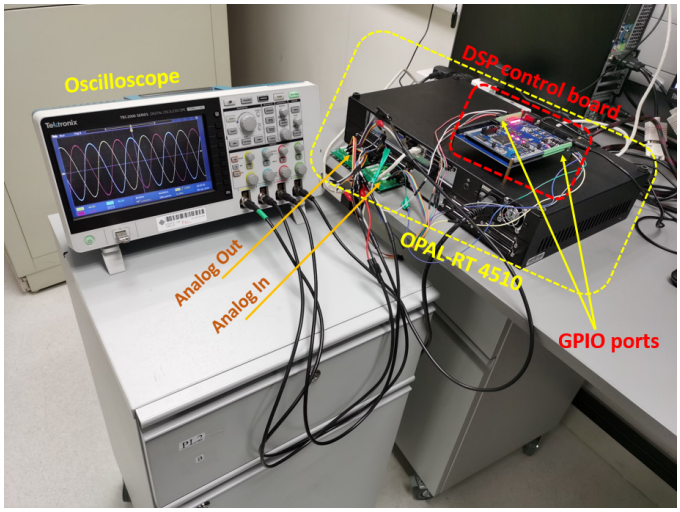

Fig.15 The RT-Lab experiment photo

The DSP chip collects the real-time information of the three-phase Z-source inverter's operation including the currents and voltages of each node through the analog-output interface on RT-Lab. The DSP adjusts the value of parameters ***M*** and ***B*** according to the proposed algorithm. The six gate signals of the inverter are sent into the RT-Lab to control the three-phase Z-source inverter by GPIO0-5 ports, which belong to digital-input interface on the RT-Lab. The GPIO0/1 send gate signals for switch T_1 and T_2. The GPIO2/3 send gate signals for switch T_3 and T_4. The GPIO4/5 send gate signals for switch T_5 and T_6. The ADCINA0 port collects output phase voltage signal V_{La}. The model in RT-Lab and the proposed closed-loop control method in the DSP chip could be manipulated and revised via the host computer. The oscilloscope is connected to the I/O interface on RT-Lab to observe and record the waveforms or other information of the three-phase Z-source inverter. Detailed parameters of the experiments are presented in Table II.

TABLE II. PARAMETERS OF EXPERIMENTS IN RT-LAB

Items	Values
Input DC Voltage	500V
Rated Output Phase Voltage (peak)	1060.7V
Rated Output Phase Voltage (r.m.s.)	750V
Switching Frequency	10kHz
Inductance of Lz_1, Lz_2	280μH
Capacitance of Cz_1, Cz_2	141μF
Inductance of L_f	8.95mH
Capacitance of C_f	7μF
Load Resistance per Phase R_{load}	112.5Ω
Rated Output Power P_{load}	15kW

B. Experiment Results and Analysis

Experimental waveforms in steady state are shown and analyzed here. In Fig. 16, the upper and middle curves represent the gate signals of switches T_1 and T_2 in the same bridge. The bottom curve represents shoot-through states which are overlaps of the two gate signals. Fig. 17 shows the three-phase output phase voltage waveforms at rated power. It is clear that there is little distortion in these waveforms with a THD of only 2.23%.

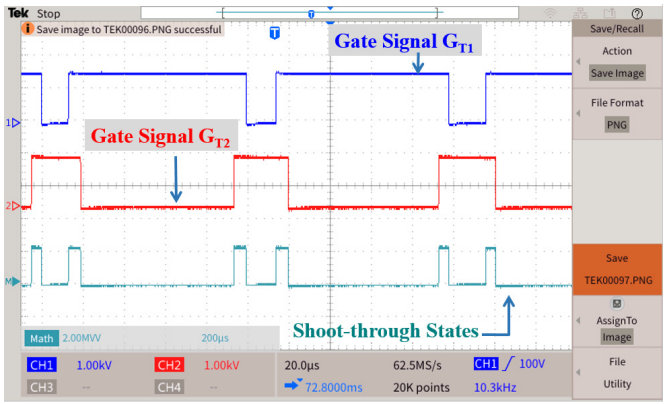

Fig. 16 Gate signals for switches T_1, T_2 and shoot-through states

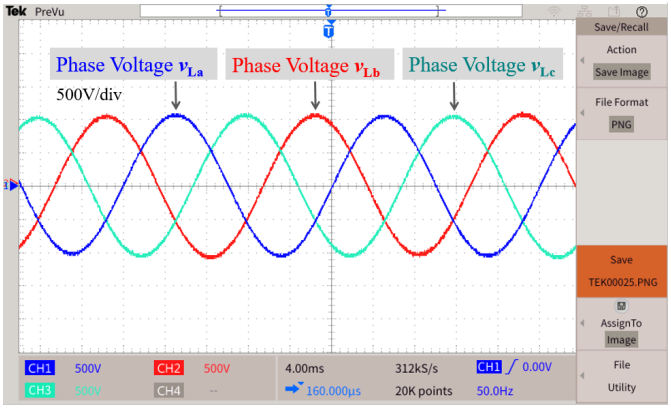

Fig. 17 Experimental waveforms of output phase voltages V_{La}, V_{Lb} and V_{Lc}

Fig. 18 shows the voltage and current of Z-source inductor L_{Z1} and capacitor C_{Z1}. Because of the symmetric topology, the waveforms are the same as the ones of another inductor L_{Z2} and capacitor C_{Z2}. The voltage pulses of $\boldsymbol{V_{LZ1}}$ come from the insertion of shoot-through states. During shoot-through states, inductor current $\boldsymbol{I_{LZ1}}$ increases rapidly and energy is stored into the inductors from both the capacitors as well as the input voltage source.

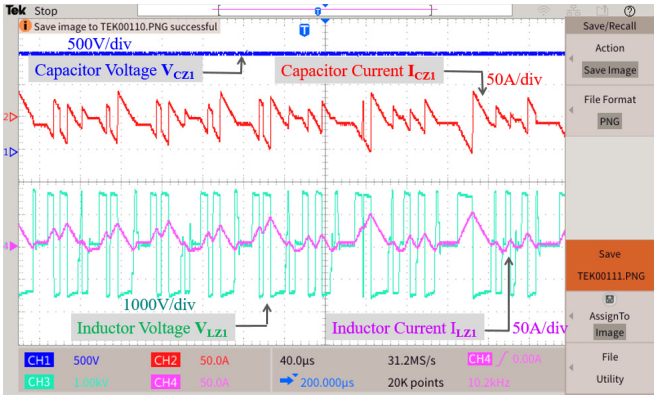

Fig.18 Voltage and current of C_{Z1} and L_{Z1}

This article has been accepted for publication in a future issue of this journal, but has not been fully edited. Content may change prior to final publication. Citation information: DOI 10.1109/TTE.2020.2984420, IEEE Transactions on Transportation Electrification

During non-shoot-through states, the inductor current I_{LZ1} decreases to a low level and becomes stable until the next shoot-through state. In this period, the inductor current is the same with the sum of capacitor current and the current injected into the three-phase full-bridge inverter I_Z. During shoot-through states, the capacitor C_{Z1} is being discharged rapidly. In non-shoot-through states, the capacitor is being charged firstly, then begins to discharge as the inductor current decreases. The capacitor voltage C_{Z1} is stable and the ripple is negligible.

Fig. 19 shows the waveforms of input current I_{in} and voltage V_Z. The input diode is reverse-biased during the shoot-through states, so the input current is zero. In non-shoot-through states, the diode is forward biased [33] and current flows from the DC voltage source into the Z-source inverter. The current then drops to zero when V_{CZ1}-V_{LZ2}=V_{dc}. The maximum magnitude of V_Z is equal to $2V_{CZ1}$-V_{dc} as described in (3). In shoot-through states, V_Z becomes zero. The average value V_Z is equal to the capacitor voltage V_{CZ1} or V_{CZ2}.

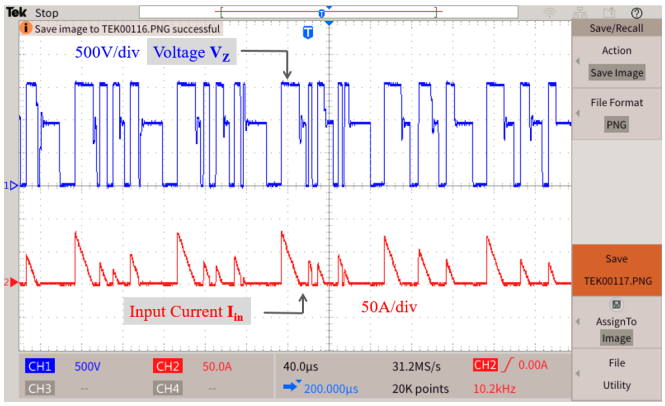

Fig.19 Experimental waveforms of voltage V_Z and input current I_{in} in steady state

The input current spikes of three-phase Z-source inverter could be harmful to the batteries, and therefore shall be suppressed to within an acceptable level by reducing the shoot-through state duty cycle D and the capacitance C_Z. There is a compromise between the output voltage boost ratio and the peak magnitude of input current spike. As shown in Fig. 19, the peak magnitude of input current is about 90A which is about 3 times of its average magnitude 30A. While the 90A current spike is acceptable for popular EV batteries in the markets which are capable of 200A continuous output current in discharging mode [39] [40], the suppression of input current spikes deserves further research in future.

Since the sine variable modulation is developed into a closed-loop PI control, three closed-loop experiments were conducted to testify the transient performance of the converter with step changes in output voltage reference, load resistance and input voltage as the disturbances.

First, transient waveforms of output voltage when the maximum amplitude of voltage reference changes from 1060V to 1400V is presented in Fig. 20. The waveforms represent phase voltages V_{La}, V_{Lb} and V_{Lc} respectively. A signal curve showing the change of reference voltage is also displayed. It is clear that phase voltages increase to the new reference magnitude smoothly within six cycles.

Thirdly, the input voltage source is regarded as the disturbance. The input voltage increases from 500V to 600V in

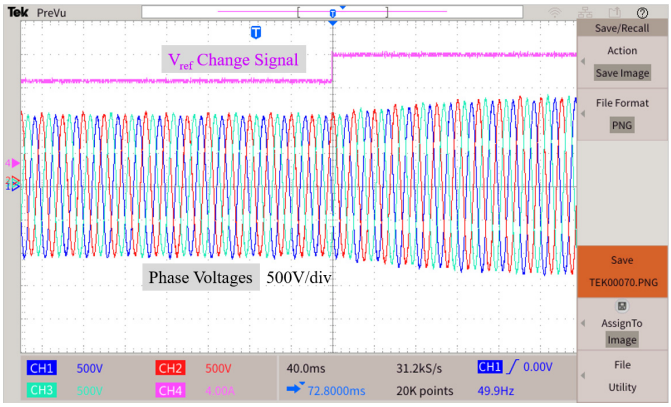

Fig.20 Transient waveforms when output voltage reference changes

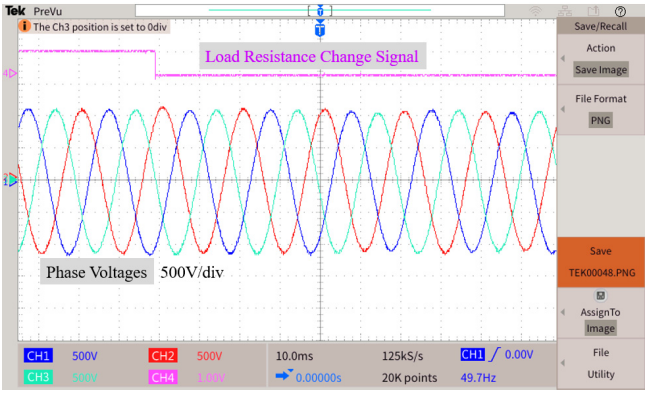

(a)

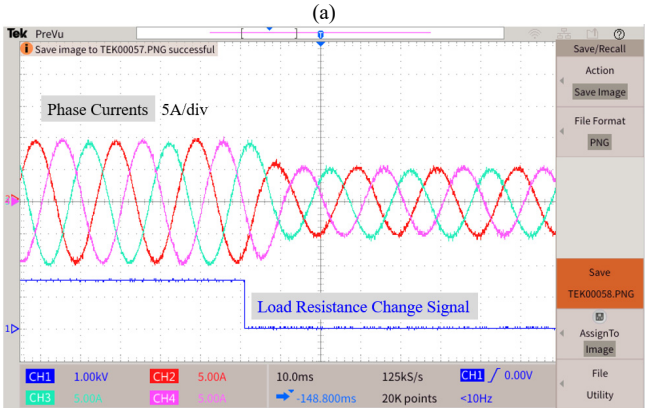

(b)

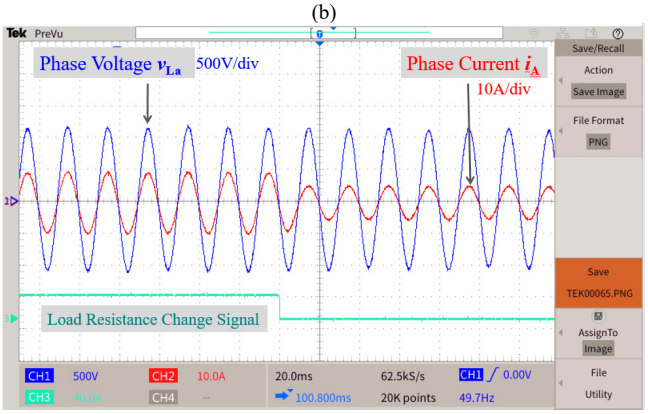

(c)

Fig.21 Transient waveforms when load resistance changes: (a) Output phase voltages; (b) Output currents; (c) Phase voltage V_{La} and current I_A

the experiment. Fig. 22 shows an overall view of the transient waveforms when the input voltage increases. It is obvious that the output phase voltage are stable during the disturbance of

This article has been accepted for publication in a future issue of this journal, but has not been fully edited. Content may change prior to final publication. Citation information: DOI 10.1109/TTE.2020.2984420, IEEE Transactions on Transportation Electrification

input voltage magnitude. In contrast, voltage V_Z decreases when the input voltage V_{in} increases. When V_{in} increases, the closed-loop control scheme will reduce the value of B to insert less shoot-through states so as to maintain the reference magnitude of output phase voltages. The average value of V_Z is also unchanged, which directly determines the magnitude of output phase voltages, but the duty ratio of shoot-through states becomes smaller. As described before, V_Z reduces to zero during shoot-through states. Therefore, the maximum value of V_Z becomes smaller, as shown in Fig. 22. This experiment proves that the output phase voltages could be regulated well under the disturbance of input voltage.

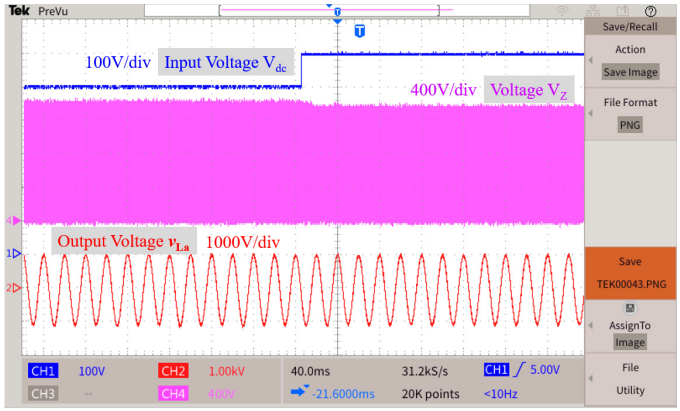

Fig.22 Transient waveforms when input voltage changes

For closed-loop experiments, the waveforms of input voltage rise, reference voltage increase and load resistance increase are presented above. In contrast, the waveforms of input voltage drop, reference voltage decrease and load resistance decrease are not presented here to conserve the space, as their results are similar and symmetric with the same conclusions to be drawn.

Secondly, the load resistance changes from 112.5Ω to 200Ω while the voltage reference is constant at 1060V. The output phase voltages and output phase currents are presented in Fig. 21(a) and Fig. 21(b). The change of load resistance is indicated by a signal curve. In Fig. 21(c), phase voltage V_{La} and the corresponding current I_A are presented together. It is clear that at the moment of load resistance change, there is a disturbance of the phase voltages. Afterward, the phase voltages become stable and catch the reference well. The currents reduce because of the increase of load resistance. It proves that the output phase voltages could be regulated when the load resistance varies.

In short, the experiment results match well with the proposed control theory and simulation results. The voltage-boosting capability of the sine variable closed-loop control method is proved with little harmonics and uncomplicated control algorithm compared to existing methods [27]. When the voltage reference changes, the output voltage could smoothly and quickly track and catch the reference. The proposed control method is also capable of stable operation under the disturbance of load resistance and input voltage.

V. Conclusion

The theoretical analysis, simulation and experimental results in the paper proved the good performance of the proposed methods for bi-directional three-phase Z-source converters. Shoot-through states are inserted sinusoidally, and the output three-phase voltages could be boosted while the harmonics are maintained within a low level. Constant variable method, sine variable method and cosine variable method are introduced and compared. Sine variable method produces least harmonics, and hence is further developed into a closed-loop PI control method. Steady-state waveforms in experiment results proved the capability of voltage boosting with all circuitry waveforms matched the theoretical analysis. Transient waveforms showed the dynamic response with the disturbance of input voltage and load resistance. The output phase voltages could catch the reference quickly and smoothly. Compared to existing control methods, the proposed one has better performance on harmonics suppression with an uncomplicated control algorithm, thus would be suitable for its application in vehicle chargers with bi-directional power flow between the vehicle batteries and the three-phase AC bus of a microgrid. The future work mainly includes the implementation of an EV charger prototype to testify the charging performance and conversion efficiency in a Power Hardware-In-Loop (PHIL) testing platform, suppression of the input current spikes and the advanced control in unbalanced load cases.

Appendix

A. Equivalent Circuits

Circuit diagrams of three-phase Z-source inverters in different modes are shown in Fig. 23. In shoot-through states, the three-phase full bridge is short-circuited, so the voltage across the Z-source topology V_Z=0. As shown in Fig. 23(a), shoot-through states are realized by switch T_1 and T_2 for example. The bolded blue lines show the current flow. The capacitors C_{Z1} and C_{Z2} are being discharged. The diode D_r is reversely biased because the voltage across the C_{Z1} and C_{Z2} is greater than input DC voltage. The following equations could be obtained by applying Kirchhoff Laws.

$$\begin{cases} v_{LZ1} = v_{CZ1} = v_{LZ2} = v_{CZ2} \\ i_{LZ1} + i_{CZ1} = i_{LZ2} + i_{CZ2} = 0 \\ i_Z = i_{LZ1} - i_{CZ2} = i_{LZ2} - i_{CZ1} \end{cases} \tag{13}$$

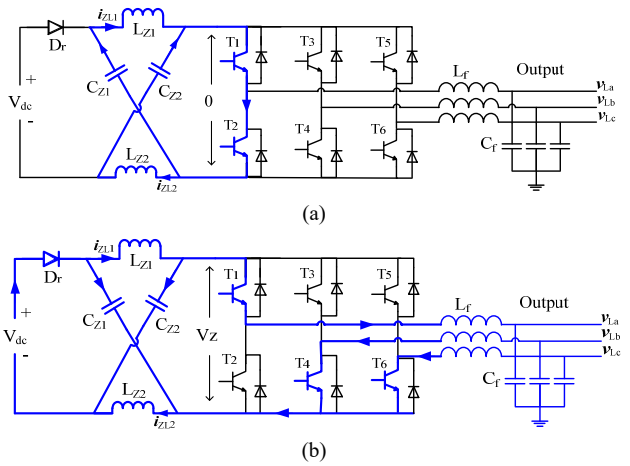

Fig. 23 Equivalent circuit of the converter in different modes: (a) Shoot-through states when T_1 and T_2 is turned on; (b) Non-shoot-through states when T_1, T_4 and T_6 is turned on

In non-shoot-through states, the diode D_r is forward biased as shown in Fig. 23(b). The current loop T_1-T_4-T_6 is highlighted

by bolded blue lines as an example. The capacitors C_{Z1} and C_{Z2} are being charged by the input DC voltage source. Similarly, the following equations could be obtained.

$$\begin{cases} v_{LZ1} = v_{LZ2} = V_{dc} - v_{CZ1} = V_{dc} - v_{CZ2} \\ V_Z = 2v_{CZ1} - V_{dc} \\ i_{LZ1} = i_{CZ2} + i_Z \\ i_{LZ2} = i_{CZ1} + i_Z \end{cases} \tag{14}$$

Equations (2) and (3) could then be derived by combining equations (13) and (14).

B. Parameters Calculation in Simulations and Experiments

The equations for designing inductance and capacitance parameters of the Z-source inverter are presented below. With regard to the Z-source inductors L_{Z1}, L_{Z2} and capacitors C_{Z1} and C_{Z2}, the design principles are restricting the ripples of inductor current and capacitor voltage.

$$C_Z = \frac{i_{CZ} \cdot dt}{dV_{CZ}} = \frac{\overline{i_{LZ}} \cdot D}{\alpha \overline{V_{CZ}} f_s} \tag{15}$$

$$L_Z = \frac{V_{LZ} \cdot dt}{dI_{LZ}} = \frac{\overline{V_{CZ}} \cdot D}{\beta \overline{I_{Lz}} f_s} \tag{16}$$

In equations (15) and (16), α represents the ratio of capacitor voltage ripple by average capacitor voltage, β represents the ratio of inductor current ripple by average inductor current, D represents the rated duty ratio of shoot-through states, and f_s represents switching frequency. In this paper, f_s=10kHz and α=β=D=0.1, which means the expected ripples of I_L and V_C account for 10% of their average values.

With regard to the LC filter, a cut-off frequency is set as 2kHz, which is equivalent to 20% of the switching frequency. The equations for the inductance and capacitance are:

$$L_f = \sqrt{\frac{\frac{\omega_1 U_o^{\,2}}{\omega_L^{\,2}} + \frac{\omega_1^{\,3} U_o^{\,2}}{\omega_L^{\,4}}}{\omega_1 I_o^{\,2}}} \tag{17}$$

$$C_f = \frac{1}{\omega_L^{\,2} \cdot L_f} \tag{18}$$

where U_o and I_o represent rated output voltage and current, ω_1 represents the angular frequency of modulation wave, ω_L represents the angular cutting-off frequency [41]. The above parameters might be further adjusted when conducting the frequency response analysis and PI settings in order to guarantee a dynamic performance of the closed-loop control.

REFERENCES

[1] S. A. Singh, G. Carli, N. A. Azeez and S. S. Williamson, "A modified Z-source converter based single phase PV/grid inter-connected DC charging converter for future transportation electrification," *2016 IEEE Energy Conversion Congress and Exposition (ECCE)*, Milwaukee, WI, 2016, pp. 1-6.

[2] Yushan Liu, Haitham Abu-rub, Gaoming Ge, "Z-Source Quasi Z Source Inverters Derived Networkds Modulations", *IEEE Industrial Electronics Magazine*, Dec 2014

[3] S. Jain, M. B. Shadmand and R. S. Balog, "Decoupled Active and Reactive Power Predictive Control for PV Applications Using a Grid-Tied Quasi-Z-Source Inverter," *IEEE Journal of Emerging and Selected Topics in Power Electronics*, vol. 6, no. 4, pp. 1769-1782, Dec. 2018.

[4] Fang Zheng Peng, "Z-source inverter," *IEEE Transactions on Industry Applications*, vol. 39, no. 2, pp. 504-510, March-April 2003.

[5] Miaosen Shen, Jin Wang, A. Joseph, Fang Zheng Peng, L. M. Tolbert and D. J. Adams, "Constant boost control of the Z-source inverter to minimize current ripple and voltage stress," *IEEE Transactions on Industry Applications*, vol. 42, no. 3, pp. 770-778, May-June 2006.

[6] Y. Liu, H. Abu-Rub, Y. Xue and F. Tao, "A Discrete-Time Average Model-Based Predictive Control for a Quasi-Z-Source Inverter," *IEEE Transactions on Industrial Electronics*, vol. 65, no. 8, pp. 6044-6054, Aug. 2018.

[7] Q. Zhang, T. Na, L. Song and S. Dong, "A Novel Modulation for Soft-Switching Three-Phase Quasi-Z-Source Rectifier Without Auxiliary Circuit," *IEEE Transactions on Industrial Electronics*, vol. 65, no. 6, pp. 5157-5166, Jun. 2018.

[8] Guo Feng, Fu Lixing, Lin, Chien Hui, Li Cong, Choi Woongchul, Wang Jin, "Development of an 85-kW Bidirectional Quasi-Z-Source Inverter With DC-Link Feed-Forward Compensation for Electric Vehicle Applications", *IEEE Transactions on Power Electronics*, vol. 28, no. 12, pp. 5477-5488. Dec 2013

[9] Tuopu Na, Qianfan Zhang, Jiaqi Tang, and Jinxin Wang, "Active Power Filter for Single-Phase Quasi-Z-Source Integrated On-Board Charger", *CPSS Transactions on Power Electronics and Applications*, vol. 3, no. 3, Sep 2018

[10] Alexandre Battiston, El-Hadj Miliani, Serge Pierfederici, and Farid Meibody-Tabar, "Efficiency Improvement of a Quasi-Z-Source Inverter-Fed Permanent-Magnet Synchronous Machine-Based Electric Vehicle," *IEEE Transactions on Transportation Electrification*, vol. 2, no. 1, pp. 14-23, 2016.

[11] Jérémy Cuenot, Sami Zaim, Babak Nahid-Mobarakeh, et al, "Overall Size Optimization of a High-Speed Starter Using a Quasi-Z-Source Inverter," *IEEE Transactions on Transportation Electrification*, vol. 3, no. 4, pp. 891-900, Dec 2017.

[12] Y. Li, S. Jiang, J. G. Cintron-Rivera and F. Z. Peng, "Modeling and Control of Quasi-Z-Source Inverter for Distributed Generation Applications," *IEEE Transactions on Industrial Electronics*, vol. 60, no. 4, pp. 1532-1541, April 2013.

[13] W. Liang, Y. Liu, B. Ge, H. Abu-Rub, R. S. Balog and Y. Xue, "Double-Line-Frequency Ripple Model, Analysis, and Impedance Design for Energy-Stored Single-Phase Quasi-Z-Source Photovoltaic System," *IEEE Transactions on Industrial Electronics*, vol. 65, no. 4, pp. 3198-3209, April 2018.

[14] H. Zeng, X. Wang and F. Z. Peng, "High power density Z-source resonant wireless charger with line frequency sinusoidal charging," *2017 IEEE Energy Conversion Congress and Exposition (ECCE)*, Cincinnati, OH, 2017, pp. 2773-2778.

[15] Tianfeng Wang, Xin Liu, Houjun Tang and Muhammad Ali, "Modification of the wireless power transfer system with Z-source inverter," *Electronics LETTERS*, vol. 53, no. 2, pp. 106-108, Jan 2017

[16] D. He, W. Cai and F. Yi, "A power decoupling method with small capacitance requirement based on single-phase quasi-Z-source inverter for DC microgrid applications," *2016 IEEE Applied Power Electronics Conference and Exposition (APEC)*, Long Beach, CA, 2016, pp. 2599-2606.

[17] D. Keshavarzi, T. Ghanbari and E. Farjah, "A Z-Source-Based Bidirectional DC Circuit Breaker With Fault Current Limitation and Interruption Capabilities," *IEEE Transactions on Power Electronics*, vol. 32, no. 9, pp. 6813-6822, Sep. 2017.

[18] Amir Hakemi, Mohammad Monfared, "Very high gain three-phase indirect matrix converter with two Z-source networks in its structure", IET Renewable Power Generation, vol. 11, no. 5, Apr 2017

[19] A. Narula and V. Verma, "Bi-directional trans-Z source boost converter for G2V/V2G applications," *2017 IEEE Transportation Electrification Conference (ITEC-India)*, Pune, Dec 2017, pp. 1-6.

[20] X. Jia, G. Chuai, H. Niu and Q. Zhang, "Grid Connected Power Generation Control Method for Z-Source Integrated Bidirectional Charging System," *2018 International Power Electronics Conference (IPEC-Niigata 2018 -ECCE Asia)*, Niigata, 2018, pp. 3025-3029.

[21] Y. Liu, B. Ge, H. Abu-Rub and F. Z. Peng, "Overview of Space Vector Modulations for Three-Phase Z-Source/Quasi-Z-Source Inverters," *IEEE Transactions on Power Electronics*, vol. 29, no. 4, pp. 2098-2108, April 2014.

[22] F. Gao, P.C. Loh, D. Li, F. Blaabjerg, "Asymmetrical and symmetrical embedded Z-source inverters," *IET Power Electronics*, vol. 4, no. 2, pp. 181-193, 2011

[23] Ebrahim Babaei, Elias Shokati Asl, Mohsen Hasan Babayi, Sara Laali, "Developed embedded switched-Z-source inverter," *IET Power Electronics*, vol. 9, no. 9, pp. 1828-1841, 2016.

[24] X. Fang, B. Ma, G. Gao and L. Gao, "Three phase trans-Quasi-Z-source inverter," *CPSS Transactions on Power Electronics and Applications*, vol. 3, no. 3, pp. 223-231, Sept. 2018.
[25] Liu Hongchen, Ji Yuliang, Zhao Dan, Chengming Zhang, Patrick Wheeler, Fan Guolei, "Z-source matrix rectifier," *IET Power Electronics*, vol. 9, no. 13, pp. 2580-2590, May 2016
[26] M. S. Diab, A. A. Elserougi, A. M. Massoud, A. S. Abdel-Khalik and S. Ahmed, "A Pulsewidth Modulation Technique for High-Voltage Gain Operation of Three-Phase Z-Source Inverters," *IEEE Journal of Emerging and Selected Topics in Power Electronics*, vol. 4, no. 2, pp. 521-533, June 2016.
[27] A. Abdelhakim, P. Davari, F. Blaabjerg and P. Mattavelli, "An improved modulation strategy for the three-phase Z-source inverters (ZSIs)," *2017 IEEE Energy Conversion Congress and Exposition (ECCE)*, Cincinnati, OH, 2017, pp. 4237-4243.
[28] A. Ayad, P. Karamanakos and R. Kennel, "Direct Model Predictive Current Control Strategy of Quasi-Z-Source Inverters," IEEE Transactions on Power Electronics, vol. 32, no. 7, pp. 5786-5801, July 2017.
[29] D. Xinping, Q. Zhaoming, X. Yeyuan, and F. Z. Peng, "A novel ZVS Z-source rectifier," Proc. 21st Annu. *IEEE Appl. Power Electron. Conf. Expo.*, 2006, pp. 951–955.
[30] J. Zhang, "Unified control of Z-source grid-connected photovoltaic system with reactive power compensation and harmonics restraint: design and application," *IET Renewable Power Generation*, vol. 12, no. 4, pp. 422-429, 19-Mar-2018.
[31] B. Barathy, A. Kavitha and T. Viswanathan, "Effective space vector modulation switching sequence for three phase Z source inverters," *IET Power Electronics*, vol. 7, no. 11, pp. 2695-2703, 11 2014.
[32] A. Abdelhakim, P. Davari, F. Blaabjerg and P. Mattavelli, "Switching Loss Reduction in the Three-Phase Quasi-Z-Source Inverters Utilizing Modified Space Vector Modulation Strategies," *IEEE Transactions on Power Electronics*, vol. 33, no. 5, pp. 4045-4060, May 2018.
[33] W. Xu, M. Liu, J.W. Liu, K.W. Chan, K.W. Eric Cheng, "A series of new control methods for single-phase Z-source inverters and the optimized operation," *IEEE Access*, vol. 7, pp. 113786-113800, 2019.
[34] W. Xu, K. W. Chan, N. H. L. Chan and J. Liu, "A modified control method for bi-directional Z-source converters," *2016 IEEE Transportation Electrification Conference and Expo (ITEC)*, Dearborn, MI, 2016.
[35] A. Abdelhakim, F. Blaabjerg and P. Mattavelli, "Modulation Schemes of the Three-Phase Impedance Source Inverters—Part I: Classification and Review," *IEEE Transactions on Industrial Electronics*, vol. 65, no. 8, pp. 6309-6320, Aug. 2018.
[36] A. Abdelhakim, F. Blaabjerg and P. Mattavelli, "Modulation Schemes of the Three-Phase Impedance Source Inverters—Part II: Comparative Assessment," *IEEE Transactions on Industrial Electronics*, vol. 65, no. 8, pp. 6321-6332, Aug. 2018.
[37] *IEEE Standard for Interconnection and Interoperability of Distributed Energy Resources with Associated Electric Power Systems Interfaces*, IEEE Standard 1547, 2018.
[38] T. Ma, M. H. Cintuglu and O. A. Mohammed, "Control of a Hybrid AC/DC Microgrid Involving Energy Storage and Pulsed Loads," *IEEE Transactions on Industry Applications*, vol. 53, no. 1, pp. 567-575, Jan.-Feb. 2017.
[39] EVTV Monitor/Controller For Tesla Model S Battery Modules. Accessed: 10 Jan, 2020. [online]. Avaliable: http://media3.ev-tv.me/TeslaModuleController.pdf
[40] BYD Fe Battery for HEV/EV, Accessed on 10 Jan, 2020 [online], Avaliable: http://www.produktinfo.conrad.com/datenblaetter/250000-274999/251704-in-01-en-BYD_LITHIUM_FE_BLOCK_12V_10_AH_B_BMS.pdf
[41] L. HE, J.S. Wang, "A design approach of LC Filter used to Three-phase PWM Inverter Output," *Electric Drive*, vol. 43, no. 12, pp. 33-37, 2013.

Wenzheng Xu received the B.Eng. degree in electrical engineering from Beijing Jiaotong University, Beijing, China, in 2012, the M.Sc. degree in electrical and electronic engineering from The University of Hong Kong, Hong Kong, in 2013, and the Ph.D. degree in electrical engineering from The Hong Kong Polytechnic University (PolyU), Hong Kong, in 2020. He was a Research Assistant with the Department of Electrical Engineering, PolyU, from September 2013 to June 2015. He is currently a Postdoctoral Fellow with the Department of Electrical Engineering, PolyU, working on high-power converters and fast-charging devices for electric vehicles. His research interests include power electronics topologies, dual-active-bridge converters, bi-directional Z-source converters, control of switch-mode converters, and their applications in microgrids.

Ka Wing Chan (M'98) received the B.Sc. (First Class Honors) and Ph.D. degrees in electronic and electrical engineering from the University of Bath, U.K., in 1988 and 1992, respectively. He currently is an Associate Professor and Associate Head with the Department of Electrical Engineering of The Hong Kong Polytechnic University. His general research interests include power system stability, analysis and control, power grid integration, security, resilience and optimization, demand response management, etc.

Siu Wing Or received the B.Sc. (First Class Honors), M.Phil., and Ph.D. degrees in engineering physics from The Hong Kong Polytechnic University (PolyU), Hong Kong, in 1995, 1997, and 2001, respectively. He was a Teaching Company Associate, a Research Electronic Engineer, and a Senior Research Electronic Engineer with ASM Pacific Technology Ltd., Hong Kong, from 1995 to 2001. He was a Postdoctoral Research Fellow with the Mechanical and Aerospace Engineering Department, University of California at Los Angeles, Los Angeles, CA, USA, for one and a half years, before he joined PolyU as a Lecturer in 2002. He currently is a Professor, the Director of Smart Materials and Systems Laboratory, and the Director of Electrical Protection and High Voltage Coordination Laboratory with the Department of Electrical Engineering, PolyU. His research interests include smart materials and devices in the bulk, micro, and nanoscale, electrical condition monitoring, electromagnetic absorption and shielding, and energy harvesting, storage, and management. He has authored or coauthored more than 300 publications, including 2 professional book chapters, more than 200 SCI journal papers, more than 100 international conference papers, in addition to the award of 43 patents.

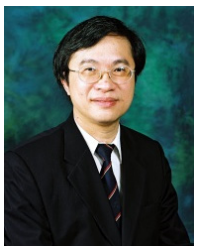

S. L. Ho received the B.Sc. and Ph.D. degrees in electrical engineering from the University of Warwick, Coventry, U.K., in 1976 and 1979, respectively. He has been with the Department of Electrical Engineering, The Hong Kong Polytechnic University, Hong Kong, since 1979, where he is currently the Associate Vice President (Academic Support) cum Registrar and the Chair Professor of Electricity Utilization. His research interests include condition monitoring of railway systems, novel sensors, optimization of electromagnetic devices, phantom loading of electrical machines, and design and development of novel machines. He has authored or coauthored more than 350 papers in SCI journals, mostly in IEEE Transactions and the Institute of Engineering and Technology Proceedings, more than 300 international conference papers, and holds several patents. Prof. Ho is a member of the Hong Kong Institution of Engineers.

Ming Liu received his B.Eng. degree in electrical engineering from Qingdao University, Qingdao, China, in 2014, and received his Ph.D. degree in electrical engineering at The Hong Kong Polytechnic University (PolyU), Hong Kong, in 2020. He is currently a Postdoctoral Fellow with the Department of Electrical Engineering, PolyU, working on intelligent control algorithms for motor drives. His research interests include model predictive control for power converters and motor drives, and wireless power transfer.